

Theory for the atomic force microscopy of layered elastic surfaces

G Overney†, D Tománek†, W Zhong†, Z Sun†, H Miyazaki‡§, S D Mahanti† and H-J Güntherodt‡

† Department of Physics and Astronomy and Center for Fundamental Materials Research, Michigan State University, East Lansing, Michigan 48824-1116, USA

‡ Department of Physics, University of Basel, Klingelbergstrasse 82, CH-4056 Basel, Switzerland

Received 30 April 1991, in final form 24 January 1992

Abstract. We present a first-principles theory of atomic force microscopy (AFM) on layered elastic surfaces. Substrate distortions due to the AFM tip and intercalant impurities are described within continuum elasticity theory, using elastic constants determined from *ab initio* density functional calculations. We apply this theory to graphite and calculate local distortions in the vicinity of an AFM tip and/or an intercalant atom. Using this formalism, we discuss the effect of a finite size tip (or a graphite flake attached to the tip) on the substrate distortions and the resulting AFM image. Our calculations show that the AFM should be a unique tool to determine the *local* surface rigidity and the healing length of graphite near structural impurities.

1. Introduction

Since the first presentation of the atomic force microscope (AFM) by Binnig *et al* [1, 2] in 1987, the field of surface imaging has experienced rapid development. Several groups have achieved atomic resolution on highly oriented pyrolytic graphite (HOPG) [3–5]. The power of the AFM lies in its ability to resolve isolated atomic defect structures such as steps or impurity atoms on both conducting and insulating surfaces. Like the better established scanning tunnelling microscope (STM) [6], the AFM uses an ‘atomically’ sharp tip which scans the sample surface at a sample-to-tip separation of a few angstroms. The AFM probes the substrate structure by measuring the equilibrium tip height z_t during a horizontal scan of the surface along x for a constant preset external force (load) F_{ext} applied to the tip. The force between the AFM tip and the substrate is measured directly from the deflection of a soft cantilever supporting the tip.

Present theories of AFM have so far calculated the force acting between a semi-infinite ‘periodic’ tip with a rigid surface [7] or a single tip interacting with a model system of finite thickness [8, 9]. In this paper, we determine the interaction between an AFM tip and an elastic semi-infinite surface from first principles. We give a detailed description of the corresponding theory, which also underlies our recent letter on this subject [10], and show how it can be improved and extended to new applications.

§ Permanent address: Department of Applied Physics, Tohoku University, Sendai 980, Japan.

Since a first-principles calculation of long-range distortions near isolated impurities in extended systems is computationally intractable at present, we develop a new general approach to this problem. We first use *ab initio* calculations to determine the elastic response of the substrate to external forces. In a second step, we use this information in the framework of the continuum elasticity theory to determine deformations near structural impurities [10, 11]. This procedure allows for a fairly simple adaptation of the formalism to a variety of geometries which are computationally beyond the scope of a first-principles calculation (e.g., the dilute limit).

This paper is organized as follows. The theoretical formalism is outlined in section 2. Computational details and results for a 'perfect' AFM interacting with graphite are presented in section 3. The special case of a graphite flake attached to the AFM tip is discussed in section 4. Finally, in section 5, we summarize our results and present conclusions.

2. Theory

2.1. Density functional calculations

The elastic response of a solid to external forces can be obtained from first-principles total energy calculations within the density functional theory [12, 13]. We use the local density approximation (LDA) to this theory [13] which expresses the total energy of the system in the ground state by

$$E_{\text{tot}} = \sum_{\text{occ}} \epsilon_{n,k} - \frac{1}{2} \int d\mathbf{r} V_{\text{H}}(\rho)\rho - \int d\mathbf{r} V_{\text{xc}}(\rho)\rho + \int d\mathbf{r} \epsilon_{\text{xc}}(\rho)\rho + E_{\text{ion-ion}}. \quad (1)$$

Here, V_{H} is the Hartree potential due to the electron charge density ρ and V_{xc} is a local exchange–correlation potential which is conventionally taken from a first-principles calculation of the electron gas. $\epsilon_{\text{xc}}(\rho)\rho$ is the exchange–correlation energy density and $E_{\text{ion-ion}}$ is the electrostatic repulsion energy between the bare ions. The correct electron density ρ and the LDA eigenvalues $\epsilon_{n,k}$ in the ground state are obtained by solving the Kohn–Sham equations self-consistently [13]

$$\left(-\frac{\hbar^2}{2m} \nabla^2 + V_{\text{ion}}(\mathbf{r}) + V_{\text{H}}(\rho) + V_{\text{xc}}(\rho) \right) \psi_{n,k}(\mathbf{r}) = \epsilon_{n,k} \psi_{n,k}(\mathbf{r}) \quad (2)$$

and

$$\rho(\mathbf{r}) = e \sum_{\text{occ}} |\psi_{n,k}(\mathbf{r})|^2. \quad (3)$$

V_{ion} is the potential due to the ion cores which—in the case of graphite—is replaced by an *ab initio* pseudopotential generated within the scheme of Hamann *et al* [14]. The exchange–correlation energy is determined using the parametrization of Hedin and Lundqvist [15]. We expand the wave functions in a linear combination of local Gaussian-type orbitals. We use the Cartesian Gaussians of the form $x^i y^j z^k \exp(-\alpha r^2)^\dagger$. These orbitals are typically located on atomic sites. In selected

† An s-orbital is given by $\exp(-\alpha r^2)$ and the three p-orbitals are given by $x \exp(-\alpha r^2)$, $y \exp(-\alpha r^2)$, and $z \exp(-\alpha r^2)$. The combination $(x^2 + y^2 + z^2) \exp(-\alpha r^2)$ describes an s-orbital.

cases we extend our basis by floating orbitals on interstitial sites. At each C site, we consider s- and p-orbitals with three radial Gaussian decays each, i.e. twelve independent basis functions. The decays that minimize the total energy of graphite are [16, 17] $\alpha = 0.24, 0.797$ and 2.65 . We use an energy cutoff of 49 Ryd in the Fourier expansion of the charge density in order to ensure complete convergence of the LDA spectrum and total energies. The LDA charge density and potentials are obtained by sampling the Brillouin zone with a fine mesh of 245 k points, using the special-point scheme of Chadi and Cohen [18].

2.2. Elasticity theory for layered materials

It appears highly desirable to describe the elastic behaviour of graphite in a general way, using a set of coupled differential equations. In such a case we can obtain several analytic and universal results. Moreover, this approach can be used *directly* to predict AFM images with atomic-scale resolution if we identify an envelope function associated with the atomic displacements at the surface as given by the following continuum elasticity theory. We apply our formalism to graphite and determine the deformations due to intercalants and/or the AFM tip. We will show that intercalant-induced deformations can be observed by the AFM and that such images contain valuable information about the *local* surface rigidity.

We assume a semi-infinite system of graphite layers. Each graphite layer is considered as a two-dimensional elastic continuous medium, or a thin elastic plate [19]. The AFM tip is characterized by the spatial distribution of forces acting on the substrate. An isolated intercalant impurity in the first gallery is modelled by an incompressible 'stick' of finite thickness which is perpendicular to the first and second graphite layers. The semi-infinite system of graphite layers is characterized by the flexural rigidity D , transverse rigidity K (proportional to C_{44}), c -axis compressibility G (proportional to C_{33}), and the interlayer spacing d . The relations between D , K and G and the elastic tensor components are

$$K = C_{44}d_{C-C}^2 \quad G = C_{33}/d \quad D = \frac{8}{3}C_{44}h^3 \left(\frac{C_{12} + C_{44}}{C_{11}} \right) \quad (4)$$

where d_{C-C} is the in-plane C-C bond length and h is called the effective layer thickness. Since the quantity h is only meaningful in cases where h can be measured (e.g. macroscopic systems), we present a different way to express D (see (33)). The vertical distortions of the graphite layers $w_n(\mathbf{r})$ due to a general distribution of forces (originating from the AFM tip or an intercalant impurity) are solutions of the following set of partial differential equations

$$\begin{aligned} (D\nabla_{\mathbf{r}}^4 - K\nabla_{\mathbf{r}}^2)w_1 + G(w_1 - w_2) &= F_1(\mathbf{r}) \\ (D\nabla_{\mathbf{r}}^4 - K\nabla_{\mathbf{r}}^2)w_2 + G(-w_1 + 2w_2 - w_3) &= F_2(\mathbf{r}) \\ &\vdots \end{aligned} \quad (5)$$

$$(D\nabla_{\mathbf{r}}^4 - K\nabla_{\mathbf{r}}^2)w_n + G(-w_{n-1} + 2w_n - w_{n+1}) = F_n(\mathbf{r}) \quad n \geq 2.$$

The vector \mathbf{r} is two-dimensional. The set of equations (5) can be transformed into a dimensionless form using

$$l_0 \equiv \left(\frac{D}{G} \right)^{1/4} \quad \rho \equiv \frac{\mathbf{r}}{l_0} \quad \delta \equiv \frac{K}{2\sqrt{DG}} \quad (6)$$

where l_0 is a characteristic length scale defining a displacement field

$$u_n(\rho) \equiv w_n(r). \quad (7)$$

2.2.1. Deformations due to the AFM tip. Consider a cylindrical AFM tip with radius R_0 at position $r = 0$. The total external force (load) F_{ext} is evenly distributed by a constant 'hydrostatic' pressure on the substrate and acts on the first layer. The force distribution due to this tip is given by

$$F_1(r) = -\frac{F_{\text{ext}}}{\pi R_0^2} \theta(R_0 - r) \quad (8)$$

and

$$F_n(r) = 0 \quad n \geq 2. \quad (9)$$

Here, $\theta(R_0 - r)$ is the Heaviside step function

$$\theta(R_0 - r) \equiv \begin{cases} 0 & \text{if } r > R_0 \\ 1 & \text{if } r < R_0. \end{cases} \quad (10)$$

We use R_0 as a model parameter to distinguish between 'sharp' and 'dull' AFM tips. The net force applied on the surface through the tip is equal to the external load applied to the tip, $\int d\mathbf{r} F_1(r) = -F_{\text{ext}}$. Tip-induced substrate distortions due to a cylindrical force distribution are then given by

$$(\nabla_\rho^4 - 2\delta\nabla_\rho^2 + 1)u_1 - u_2 = -\frac{F_{\text{ext}}}{\pi\rho_0^2} \frac{1}{\sqrt{GD}} \theta(\rho_0 - \rho) \quad (11)$$

⋮

$$(\nabla_\rho^4 - 2\delta\nabla_\rho^2 + 2)u_n - u_{n-1} - u_{n+1} = 0 \quad n \geq 2$$

where $\rho_0 = R_0/l_0$. To solve this set of equations, we first define the Fourier transformed distortion as

$$\tilde{u}_n(q) \equiv \int d\rho e^{iq\rho} u_n(\rho). \quad (12)$$

Then, equations (11) become

$$(q^4 + 2\delta q^2 + 1)\tilde{u}_1 - \tilde{u}_2 = -\frac{2F_{\text{ext}}}{\sqrt{GD}} \frac{J_1(q\rho_0)}{q\rho_0} \quad (13)$$

⋮

$$(q^4 + 2\delta q^2 + 2)\tilde{u}_n - \tilde{u}_{n-1} - \tilde{u}_{n+1} = 0 \quad n \geq 2.$$

Here, $J_1(q\rho_0)$ is the Bessel function of order one†. For $n \geq 2$, (13) yields the recursive relation

$$\frac{\tilde{u}_n}{\tilde{u}_{n-1}} = \left(q^4 + 2\delta q^2 + 2 - \frac{\tilde{u}_{n+1}}{\tilde{u}_n} \right)^{-1} \equiv L(q). \quad (14)$$

† Equation 6.561/5 of [20] has been used when Fourier transforming.

We make the *ansatz* that the ratio $\tilde{u}_n/\tilde{u}_{n-1}$ is independent of the index n . Substituting $X(q) \equiv q^4 + 2\delta q^2 + 2$, we obtain for this semi-infinite system

$$L(q) = \frac{1}{X(q) - L(q)}. \quad (15)$$

Out of the two solutions $L(q)$ of this quadratic equation, we select the smaller root

$$L(q) = \frac{1}{2} \left\{ X(q) - [X^2(q) - 4]^{1/2} \right\}. \quad (16)$$

because $L(q)$ should vanish for large $|q|$. \tilde{u}_1 is related to \tilde{u}_n by

$$\tilde{u}_n(q) = L(q)\tilde{u}_{n-1}(q) = [L(q)]^{n-1} \tilde{u}_1(q) \quad n \geq 2. \quad (17)$$

Now, (13) and (17) can be combined to give

$$(X(q) - 1)\tilde{u}_1(q) - \tilde{u}_2(q) = -\frac{2F_{\text{ext}}}{\sqrt{GD}} \frac{J_1(q\rho_0)}{q\rho_0} \quad (18)$$

and

$$\tilde{u}_2(q) = L(q)\tilde{u}_1(q). \quad (19)$$

$\tilde{u}_1(q)$ can now be determined from

$$\tilde{u}_1(q) = -\frac{2F_{\text{ext}}}{\sqrt{GD}} \frac{J_1(q\rho_0)}{q\rho_0} (q^4 + 2\delta q^2 + 1 - L(q))^{-1}. \quad (20)$$

Combining this with (17), we obtain the corresponding expression for deeper layers,

$$\tilde{u}_n(q) = -\frac{2F_{\text{ext}}}{\sqrt{GD}} \frac{J_1(q\rho_0)}{q\rho_0} \frac{[L(q)]^{n-1}}{q^4 + 2\delta q^2 + 1 - L(q)} \quad n \geq 2. \quad (21)$$

The vertical distortion $w_n(\mathbf{r})$ in real space can be finally determined using the inverse Fourier transformation

$$w_n(\mathbf{r}) = -\frac{F_{\text{ext}}}{\pi\rho_0\sqrt{GD}} \int_0^\infty dq \frac{J_0(qr/l_0)J_1(q\rho_0)[L(q)]^{n-1}}{X(q) - 1 - L(q)} \quad n \geq 1. \quad (22)$$

In the limiting case of a rigid system (flexural rigidity $D \rightarrow \infty$) and a finite force, the layer distortions w_n are zero.

Equation (22) simplifies further in the case of a 'sharp' δ -function like tip [10], corresponding to $\rho_0 \rightarrow 0$, since

$$\lim_{\rho_0 \rightarrow 0} \frac{J_1(q\rho_0)}{q\rho_0} = \frac{1}{2}. \quad (23)$$

2.2.2. *Deformations due to an intercalant impurity.* In the next step, we consider an intercalant atom (such as K or Cs) sandwiched in the first gallery. We model this intercalant by an incompressible 'stick' of finite thickness which is perpendicular to the first and second graphite layer. The intercalant exerts a force F_{inc} on the upper and lower layer, which is evenly distributed through a constant 'hydrostatic' pressure. Let us consider the intercalant at the origin and describe the intercalant-induced substrate distortions by a force distribution similar to that of (8). In this case, in (8) F_{ext} is to be replaced by F_{inc} and R_0 by R_{inc} . In q -space, this leads to

$$\begin{aligned}\tilde{F}_1(q) &= + \frac{2F_{\text{inc}}}{\sqrt{GD}} \frac{J_1(q\rho_{\text{inc}})}{q\rho_{\text{inc}}} \\ \tilde{F}_2(q) &= - \frac{2F_{\text{inc}}}{\sqrt{GD}} \frac{J_1(q\rho_{\text{inc}})}{q\rho_{\text{inc}}} \\ &\vdots \\ \tilde{F}_n(q) &= 0 \quad n \geq 3.\end{aligned}\tag{24}$$

Here, $\rho_{\text{inc}} = R_{\text{inc}}/l_0$ and $\int d\tau F_{1,2}(\tau) = \pm F_{\text{inc}}$. In analogy to the procedure used in the above subsection describing the AFM tip only, substituting $\tilde{f}_{\text{inc}}(q) \equiv \|\tilde{F}_{1,2}(q)\|$ in (18), we get

$$\begin{aligned}(X(q) - 1)\tilde{u}_1(q) - \tilde{u}_2(q) &= \tilde{f}_{\text{inc}}(q) \\ -\tilde{u}_1(q) + (X(q) - L(q))\tilde{u}_2(q) &= -\tilde{f}_{\text{inc}}(q) \\ &\vdots \\ \tilde{u}_n(q) &= [L(q)]^{n-2} \tilde{u}_2(q) \quad n \geq 3.\end{aligned}\tag{25}$$

It can be readily be shown that,

$$\tilde{u}_1(q) = \frac{X(q) - L(q) - 1}{(X(q) - 1)(X(q) - L(q)) - 1} \tilde{f}_{\text{inc}}(q)\tag{26}$$

and

$$\tilde{u}_2(q) = \frac{2 - X(q)}{(X(q) - 1)(X(q) - L(q)) - 1} \tilde{f}_{\text{inc}}(q).\tag{27}$$

The force distribution is constructed by imposing boundary conditions on the inter-layer distance in the first gallery, or equivalently on the difference of displacements $\Delta w(\tau) = w_1(\tau) - w_2(\tau)$ in presence of the intercalant. In the absence of an AFM tip, we require that $\tau = 0$ which is the position of the intercalant,

$$\Delta w(\tau = 0) = \frac{1}{2\pi} \int_0^\infty dq \frac{\tilde{f}_{\text{inc}}(q)q(2X(q) - L(q) - 3)}{(X(q) - 1)(X(q) - L(q)) - 1}.\tag{28}$$

It is reasonable to assume that $\Delta w(\tau = 0)$ depends only on the intercalant species (size and compressibility). A possible interaction between the tip and the intercalant

(e.g. via charge transfer), which would modify this quantity, is neglected in the present discussion, but we hope to investigate this in the future [21]. In the case of an incompressible intercalant impurity, we require $\Delta w(\mathbf{r} = 0) = d_{\text{inc}} - d$, where d_{inc} is the diameter of the intercalant and d is the interlayer spacing. We can then calculate F_{inc} from (28). Once F_{inc} is known, we can determine the displacements of the first and second layer due to an intercalant by Fourier transforming (26) and (27). With the recursive equation (25), we get

$$w_1(\mathbf{r}) = \frac{F_{\text{inc}}}{\pi \rho_{\text{inc}} \sqrt{GD}} \int_0^\infty dq \frac{J_0(qr/l_0) J_1(q\rho_{\text{inc}})(X(q) - L(q) - 1)}{(X(q) - 1)(X(q) - L(q)) - 1}$$

$$\vdots$$

$$w_n(\mathbf{r}) = \frac{F_{\text{inc}}}{\pi \rho_{\text{inc}} \sqrt{GD}} \int_0^\infty dq \frac{J_0(qr/l_0) J_1(q\rho_{\text{inc}})(2 - X(q)) [L(q)]^{n-2}}{(X(q) - 1)(X(q) - L(q)) - 1} \quad (29)$$

where $n \geq 2$.

2.2.3. Deformations due to the AFM tip and an intercalant impurity. Let us consider the AFM tip and the intercalant impurity simultaneously and define their positions (with respect to the origin) as \mathbf{r}_1 and \mathbf{r}_2 , respectively. In the harmonic theory, all distortions w_n are proportional to the applied force. Consequently, the total layer distortion in the presence of an AFM tip and an intercalant is given by the linear superposition of distortions due to each of these separate interactions. If the AFM tip is at a finite distance R from the intercalant, given by $R = |\mathbf{r}_1 - \mathbf{r}_2|$, the force F_{inc} has to be adjusted in order to keep $\Delta w(\mathbf{r} = \mathbf{r}_2)$ unchanged. From now on we position the intercalant at the origin ($\mathbf{r}_2 = 0$). The modified intercalant force $F_{\text{inc}}(R)$ can be obtained from

$$\Delta w(\mathbf{r} = 0) = \Delta w^{\text{AFM}} + \Delta w^{\text{I}}. \quad (30)$$

Here, Δw^{AFM} can be obtained using the expression in (22)

$$\Delta w^{\text{AFM}} = w_1(|\mathbf{r}| = R) - w_2(|\mathbf{r}| = R) \quad (31)$$

and Δw^{I} is given by using expression (29) for the layer distortions, as

$$\Delta w^{\text{I}} = w_1(\mathbf{r} = 0) - w_2(\mathbf{r} = 0). \quad (32)$$

Of course, for $R \rightarrow \infty$, (30) reduces to (28). Once $F_{\text{inc}}(R)$ has been determined, we can calculate the deformation of each layer due to an AFM tip and an intercalant impurity using (29) and (22) and the superposition principle.

3. Computational details and results

We used a first-principles density function calculation to determine the equilibrium structure and elastic properties of graphite. Important parameters in our LDA calculation have already been described in section 2.1. We found the calculated in-plane C-C bond length $d_{\text{C-C}} = 1.42 \text{ \AA}$ to be in excellent agreement with the experimental

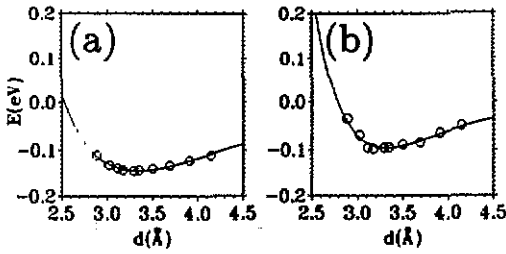


Figure 1. Binding energy of graphite (with respect to isolated layers, per carbon atom) as a function of the interlayer spacing d , (a) for hexagonal (or AB) and (b) for AA stacking of layers. The solid line represents a Morse potential fit to the calculated data points.

results. Also, the equilibrium interlayer spacing $d = 3.35 \text{ \AA}$, determined from the energy versus d curve shown in figure 1, is identical to the observed value†.

Next we calculated the frequencies of the in-plane and the out-of-plane phonon modes. As shown in figure 2(a), the in-plane E_{2g_2} mode consists of in-plane displacements of the α -sublattice with respect to the β -sublattice. The out-of-plane A_{2u} mode consists of small displacements along the c -axis of the α -sublattice with respect to the β -sublattice, as shown schematically in figure 2(b) (for this mode the C-C bond length has been kept constant). The vibration frequency can be obtained from a frozen phonon calculation, by calculating the total energy as a function of displacement.

The phonon frequencies are given by the curvature of the total energy with respect to the displacement at equilibrium. Our calculated values for the phonon frequencies are $\omega(E_{2g_2}) = 1541 \text{ cm}^{-1}$ and $\omega(A_{2u}) = 809 \text{ cm}^{-1}$. These values are in very good agreement with experimental data [22] $\omega(E_{2g_2}) = 1582 \text{ cm}^{-1}$ and $\omega(A_{2u}) = 868 \text{ cm}^{-1}$ and previously calculated values [23, 24] $\omega(E_{2g_2}) = 1598 \text{ cm}^{-1}$ and $\omega(A_{2u}) = 839 \text{ cm}^{-1}$. In our calculation, we assumed the AA layer stacking that is appropriate for stage one intercalated graphite. This explains the small difference between our results and previous experimental and theoretical data which have been obtained for regular AB stacked (hexagonal) graphite.

In the calculation of the flexural rigidity D ‡, we made the simplifying assumption that the weak interlayer interaction can be safely dropped when compared with the dominating in-plane interaction. This is true especially when the out-of-plane distortions $w(\mathbf{r})$ are very small. Hence we consider a system of decoupled graphite layers that individually obey the equation of motion [19]

$$\eta \frac{d^2 w(\mathbf{r})}{dt^2} = -D \nabla_{\mathbf{r}}^4 w(\mathbf{r}). \quad (33)$$

† In the case $d \rightarrow \infty$, the energy $E(d)$ corresponds to isolated layers. We avoided the lengthy LDA total energy calculation for an isolated graphite layer and treated it instead as a free parameter in the Morse fit. For the total energy of a monolayer we obtained -155.525 eV (figure 1(a), AB stacking) and -155.550 eV (figure 1(b), AA stacking). The small disagreement of 25 meV between these monolayer energies results from an incomplete basis in the LDA calculations. This uncertainty must be considered when comparing the absolute stability of AB versus AA stacked graphite in figure 1(a) and figure 1(b).

‡ D is related to the bending modulus B by $D = \eta B$. The proportionality constant $\eta = 2M_C/(3\sqrt{3}d_{C-C}^2/2)$ is the area mass density (in our case, M_C is the mass of a carbon atom and $d_{C-C} = 1.42 \text{ \AA}$). The experimental value for $B = (2.55 \pm 0.15) \times 10^{-5} \text{ cm}^4 \text{ s}^{-2}$ is listed in [22].

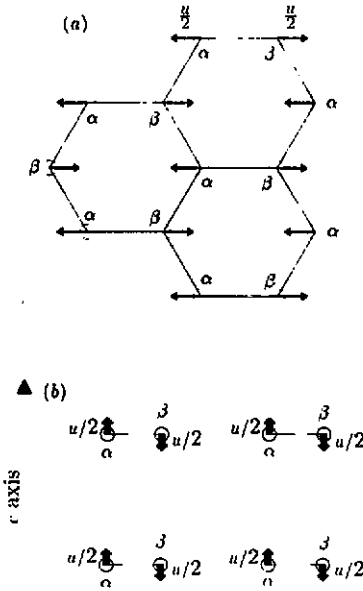


Figure 2. (a) Schematic top view of the E_{2g_2} phonon mode of graphite. In-plane displacements $u/2$ of atoms in the α - and β -sublattice are indicated by arrows. (b) Schematic side view of the A_{2u} phonon mode of graphite. Out-of-plane displacements $u/2$ of atoms in the α - and β -sublattice are indicated by arrows. The nearest-neighbour C-C bond length is kept constant.

Here, η is the area mass density. In order to determine the value of D from our first-principles calculation, we first construct a harmonic lattice spring model (see figure 3). The long-wavelength behaviour of this model corresponds to (33). Then, the total harmonic distortion energy is given by

$$E = \frac{1}{2} \gamma \sum_i \left(3u_{i1} - \sum_j 'u_{j2} \right)^2 + \frac{1}{2} \gamma \sum_i \left(3u_{i2} - \sum_j 'u_{j1} \right)^2. \quad (34)$$

In the long-wavelength limit,(34) leads to

$$\omega^2(k) = \frac{9}{16} (\gamma / M_C) k^4 d_{C-C}^4 \quad (35)$$

which is also the form of the dispersion relation obtained from (33). Here, M_C is the mass of a carbon atom and $d_{C-C} = 1.42 \text{ \AA}$. In this way, we can relate D to the microscopic force constant γ . We have determined γ from first-principles LDA calculations by creating short wavelength A_{2u} out-of-plane distortion (discussed above and shown in figure 2(b)) and comparing the LDA energy with that obtained using (34). The value of γ is $0.2584 \times 10^5 \text{ dyn cm}^{-1}$. Using this value of γ , equation (35), and the Fourier transformed (33), we can easily determine the flexural rigidity D and obtain the numerical value $D = 7589 \text{ K}$, which compares very favourably with the experimental value $D = 7076 \pm 420 \text{ K}$. We combined this value with experimental values [22] for the c -axis compressibility $G = 789 \text{ K \AA}^{-4}$ and the transverse rigidity $K = 932 \text{ K \AA}^{-2}$ in our continuum elasticity theory calculations described in section 2.2.

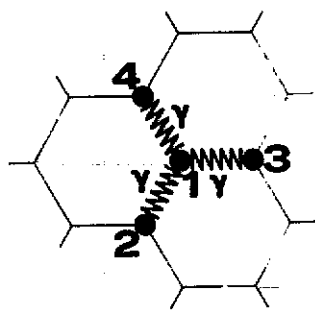


Figure 3. Schematic top view of the graphite lattice and the spring model used to describe the out-of-plane mode. The harmonic spring constant is γ .

We apply this theory first to determine the distortion of graphite layers due to the AFM tip and an intercalant impurity and present results in figure 4. The calculated equilibrium z coordinates of carbon atoms in the three topmost graphite layers near the AFM tip (solid and dotted lines) are compared with the positions of the same in the absence of external forces (dashed lines) in figure 4(a) and (c). We also investigate the effect on equilibrium geometry of local changes of the flexural rigidity D , which can occur due to charge transfer near intercalant impurities. In figure 4 we compare results for pristine graphite, obtained using $D = 7589$ K and given by solid lines, with those obtained using a reduced value $D = 3795$ K and given by dotted lines. In these calculations, we considered a cylindrical AFM tip with a radius $R_0 = 2.75$ Å. The 'hydrostatic' force distribution within R_0 is given by (8). Our calculation yields surface distortions w_n (note that $w_1 = z$ for the topmost layer†) and the healing length λ_p of pristine graphite, corresponding to the distance at which the layer distortion decreases to half its maximum value. In the linear response theory, surface distortions are proportional to the applied load F_{ext} , but the healing length should be independent of F_{ext} . Clearly, both λ_p and w_n are expected to depend on the surface flexural rigidity D .

Our results for a load $F_{\text{ext}} = 10^{-9}$ N indicate that λ_p decreases from 5.56 Å to 4.85 Å and that the maximum layer distortion z_t at the tip site $r = 0$ increases from 0.52 Å to 0.60 Å if the flexural rigidity D is reduced to half its value. Since the vertical displacement of the AFM tip $\delta z_t = z_t(F_{\text{ext}}) - z_t(F_{\text{ext}} = 0)$ due to a load depends sensitively on D , the measurement of δz_t as a function of F_{ext} should provide unique experimental access to this elastic constant and its variations along the surface. While the AFM can determine force differences to a high accuracy, the calibration of the zero-load point $F_{\text{ext}} = 0$ is very difficult and uncertain. It is useful to note in this context that within the linear elasticity theory, the value of δz_t is not affected by a miscalibration of the force by \tilde{F} , since $\delta z_t \approx z_t(F_{\text{ext}} + \tilde{F}) - z_t(\tilde{F})$ if harmonic response is assumed.

In our continuum model, the vertical position z_t of an AFM tip does not depend on its horizontal position x during a scan of the surface at constant load. In this case, the AFM image does not provide any information about the substrate distortions near the tip, shown in figure 4(a) and (c), and the healing length λ_p of graphite. The healing length can be easily probed by the AFM near a structural defect, such as a step

† The absolute vertical position z of atoms in the n th layer (with respect to the undistorted topmost layer) is given by $z(r) = -(n-1)d + w_n(r)$, where $d = 3.35$ Å is the interlayer spacing.

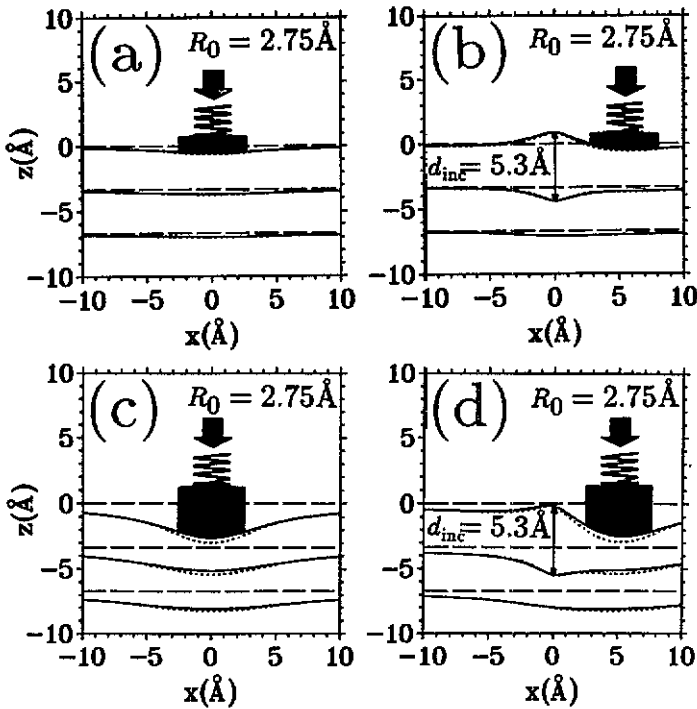


Figure 4. Equilibrium structure of graphite interacting with an AFM tip, for a load 10^{-9} N ((a) and (b)) and 5×10^{-9} N ((c) and (d)). Vertical displacements of carbon atoms in the three topmost layers are shown in a plane perpendicular to the layers, for a flexural rigidity $D = 7589$ K (solid lines) and $D = 3795$ K (dotted lines). The position of unperturbed layers is given by the dashed lines. Results for pristine graphite in (a) and (c) are compared with those for the case of a single intercalant (modelled by an incompressible infinitely thin 'stick' of length $d_{inc} = 5.3$ Å) in (b) and (d). The radius R_0 of the cylindrical AFM tip is 2.75 Å.

or an intercalant atom in the first gallery. In figure 4(b) and (d), we present results for a model intercalant representing a K atom. We use the value $d_{inc} = 5.3$ Å for the diameter of the intercalant, which is larger than the graphite interlayer spacing $d = 3.35$ Å. The force distribution of the intercalant is modelled by a pair of equal δ -function-like forces acting in opposite directions on the first and second layer. The special case of an 'infinitely thin' intercalant ($R_{inc} \rightarrow 0$) can be treated in analogy to the δ -function like tip, using (23). In figure 4(b) and (d), the horizontal distance between the AFM tip and the intercalant is assumed to be 5 Å. As in figure 4(a) and (c), the total load on the tip F_{ext} is distributed evenly on to the substrate within the tip radius $R_0 = 2.75$ Å. In figure 4(a) and (b), the load $F_{ext} = 10^{-9}$ N; in figure 4(c) and (d), $F_{ext} = 5 \times 10^{-9}$ N. Results for the topmost three layers of pristine graphite, obtained using $D = 7589$ K and given by the solid line, are compared with those obtained using a reduced value $D = 3795$ K and given by the dotted line.

The AFM image, reflecting the vertical tip position z_t as a function of the horizontal distance r_t from the intercalant, is shown in figure 5 for different AFM tip loads and tip shapes, and for a 'rigid' and a 'soft' surface. The 'rigid' surface is given

by $D = 7589$ K; and in the case of the 'soft' surface, D is chosen to be 3795 K. figure 5(a) shows the image in the case of zero load $F_{\text{ext}} = 0$, which obviously reflects the equilibrium surface structure *in the absence* of the tip. More interesting are the images obtained for a non-zero load $F_{\text{ext}} = 10^{-9}$ N applied to the surface via a δ -function AFM tip (figure 5(b)) and a cylindrical AFM tip with a constant force distribution inside the radius $R_0 = 2.75$ Å (figure 5(c)). The intercalant is modelled by an incompressible infinitely thin 'stick' in all three cases. A comparison of figures (b) and (c) confirms the intuitive result that differences between the 'rigid' and the 'soft' surface vanish gradually with increasing tip size R_0 . In general, we expect the flexural rigidity D to change in the case of charge transfer between intercalant atoms and layers in graphite intercalation compounds, in analogy to similar observed changes [23, 24] of $d_{\text{C-C}}$. Systems with intercalants should be correctly described by a locally variable $D(r)$, which shows strongest deviation from the pristine graphite value at the intercalant site $r = 0$. These local changes are partly smoothed out by a finite-size tip, and the observed AFM corrugation is expected to lie between the calculated curves for the 'soft' and 'rigid' surface.

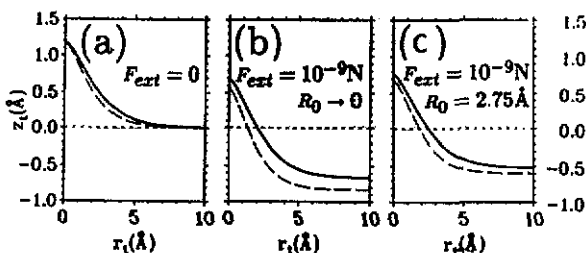


Figure 5. Vertical position z_t of the AFM tip as a function of its horizontal distance r_t from a model K intercalant atom with diameter $d_{\text{inc}} = 5.3$ Å. (a) Results for zero load on the tip for pristine graphite with $D = 7589$ K (solid line) are compared with distortions for a reduced $D = 3795$ K (dashed line). (b) Corresponding results for a load $F_{\text{ext}} = 10^{-9}$ N applied via a δ -function AFM tip. (c) Results for a load $F_{\text{ext}} = 10^{-9}$ N and a cylindrical AFM tip with a constant force distribution inside the radius $R_0 = 2.75$ Å.

The influence of the tip size on the layer distortions (and hence on the equilibrium tip position z_t) is shown in figure 6. We considered a cylindrical AFM tip with a constant 'hydrostatic' force distribution inside the variable radius R_0 , given by (8). The distortion of the topmost graphite layer at the centre of the AFM tip, $w_1(r = 0)$, is shown as a function of R_0 for two different loads ($F_{\text{ext}} = 10^{-9}$ N and 5×10^{-9} N). Results presented in figure 6 have been obtained using the flexural rigidity of pristine graphite $D = 7589$ K.

Experimental investigations of graphite intercalation compounds (GICs) using the STM or AFM are scarce at present. In STM experiments for donor GICs LiC_6 , RbC_8 , CsC_{24} , and KC_8 the exact position of the intercalants in the first gallery has been resolved in most cases [25, 26]. The corresponding AFM experiments are still in progress [27].

Once the equilibrium positions of the carbon atoms have been determined for a given force distribution, the total charge density ρ of the deformed graphite can be approximated by a superposition of atomic charge densities obtained from LDA. This approach is justified by the level of agreement between the charge densities

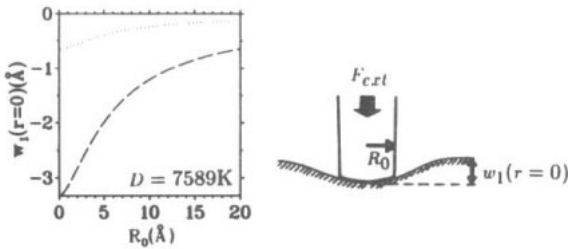


Figure 6. Distortions of the topmost graphite layer $w_1(r=0)$ at the centre of the AFM tip as a function of the effective tip radius R_0 . The total loads on the tip are $F_{\text{ext}} = 5 \times 10^{-9}$ N (dashed line) and $F_{\text{ext}} = 10^{-9}$ N (dotted line).

of undistorted graphite layers, which have been obtained from a first-principles LDA surface calculation and from superposition of atomic charge densities. These charge densities differ by less than 5%, mainly due to the incorrect description of the π -bonds in graphite as being a superposition of atomic charge densities. This small inaccuracy does not affect the corrugations that are observed in the AFM. figure 7 shows the calculated charge distribution which—in the framework of embedded-atom-like theories—is indicative of the interatomic interactions within the crystal and between an AFM tip and the substrate. The surface deformations for the applied load $F_{\text{ext}} = 10^{-9}$ N correspond to those shown in figure 4(a) and (b).

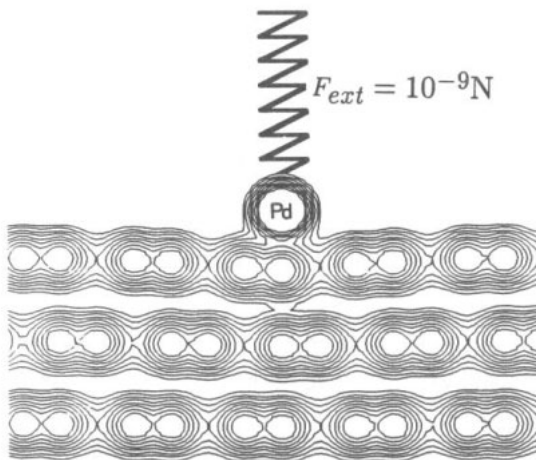


Figure 7. Total charge density ρ of a one-atom Pd AFM tip interacting with the elastic surface of hexagonal graphite near the on-top site, for a load $F_{\text{ext}} = 10^{-9}$ N. For this load, the distance between the Pd AFM tip and the graphite surface is 2.42 Å [30]. Contours of constant ρ are shown for the three topmost graphite layers in the xz plane perpendicular to the surface. The ratio of two consecutive charge density contours $\rho(n+1)/\rho(n)$ is 1.5.

Our predictions for apparent tip corrugations still hold in the presence of Van der Waals forces between the tip and the substrate. These long-range forces do not result in additional AFM corrugations and are effectively compensated in the experiment by an additional force applied on the tip suspension [28]. In order to

estimate the effect of Van der Waals forces on the AFM image, we model the AFM tip by a conus with an opening angle $\alpha = 45^\circ$. Following Anders and Heiden [29], we obtain a total Van der Waals force $F_{\text{conc}}(z) = A_{\text{H}}(\tan\alpha)^2/(6z)$, where A_{H} is the Hamaker constant for the graphite sample ($A_{\text{H}} = 3 \times 10^{-19}$ J). We find that the magnitude and site dependence of Van der Waals interactions between the AFM tip and the surface are negligible as compared with the closed-shell repulsion in the weak repulsive region (distance between AFM tip and surface smaller than about 2.5 Å). In this distance range, we obtain, for a conical tip, forces of about 0.25 nN and 0.16 nN for tip/sample separations of 2.0 Å and 3.0 Å, respectively, which are much smaller than the forces obtained from our LDA calculations published in [30]. In [30], we obtained 5.0 nN and 4.1 nN for distances of 2.0 Å and 3.0 Å, respectively. At much larger tip/sample separations, the Van der Waals forces dominate the tip-substrate interaction, but do not show measurable corrugations on the atomic scale.

4. Interaction between a graphite flake and the surface of graphite

In our theory, we have so far modelled the AFM tips either by infinitely sharp objects with a δ -function force distribution [10], or by cylinders with a constant force distribution inside a finite radius R_0 . The large cylindrical AFM tip is clearly not a very realistic description of a large AFM tip, due to the neglect of atomic structure in the tip. The assumption of a constant 'hydrostatic' distribution of the AFM load in the tip is also likely to suppress atomic-scale corrugations in the AFM images. The other limiting case of a 'sharp' AFM tip leads to considerable *local* substrate deformation even in the case of moderate loads $F_{\text{ext}} \approx 10^{-9}$ N. Loads exceeding 10^{-8} N cause a deformation beyond the elastic limit and are likely to destroy the surface [30]. Obviously, none of these models can simply explain the experimentally achieved atomic resolution on graphite for loads as large as 10^{-7} N [3].

We find two possible ways to explain this observation. First, we consider the surface covered by a protective layer (thin film) which mediates the force between a 'sharp' AFM tip and the elastic substrate [31]. The finite viscosity of the film helps to spread the AFM load across a larger area and to decrease *local* substrate deformations, hence extending the applicable force range. The atomic-scale corrugation can then be attributed to the 'floating' AFM tip. This mechanism has been used previously [31, 32] to explain apparently huge corrugations in STM images of graphite exposed to air [33, 34]. It is questionable, however, as to whether this effect can extend the apparent elastic limit of graphite by a factor of ten or more, as the value of the AFM load 10^{-7} N would suggest [3].

A second way to obtain atomic resolution for a large AFM load could be to attach a graphite 'flake' to the AFM tip. The AFM tip is likely to 'pick up' such a flake during a large-area scan of graphite. In this case, the AFM load would be effectively spread across a large substrate area since graphite behaves like a plate with a large flexural rigidity. In this case, it is obvious that the measured corrugation depends strongly on the orientation between the flake and the surface, as well as on the scan direction. The dependency of the resolution in AFM on the type and size of such multiple-atom tips has been discussed previously [30, 35]. In this section, we present numerical results for the interaction between a graphite flake and a graphite surface and investigate the atomic-scale resolution as a function of AFM load.

We model a large flake by a monolayer of graphite and determine the flake-substrate interaction from first principles. This assumption holds for large flakes

where the fraction of boundary atoms is negligible. Due to the computational complexity of the *ab initio* LDA calculations, we are limited to a few highly symmetric flake/graphite geometries which—in the bulk—correspond to a different layer stacking. Let us now consider a graphite flake perfectly aligned (in AA stacking) with the topmost graphite layer (inset in figure 8). During a horizontal AFM scan of the surface (for a scan along the C–C bond direction), the flake passes through the layer stacking sequence AA, AB, AB, AA, The latter also defines the horizontal tip position x_t as shown in figure 8. Note that all flake atoms are in the ‘on-top site’ in the AA stacking, and that every other flake atom is at the ‘hollow site’ in the AB stacking. We consider the total AFM load F_{ext} evenly distributed over the whole n -atom flake, so that the load per carbon atom in the flake is

$$f_{\text{ext}} = F_{\text{ext}}/n. \quad (36)$$

For a large flake (consisting of about 7–20 hexagons) attached to a ‘dull’ AFM tip, we ignore bending and consider the interlayer spacing between the flake and the surface as constant. Furthermore, we assume that the layer stacking of the substrate remains unchanged during the scan of the surface. This is reasonable because of the large size difference between the flake and a surface layer, and since the AFM measurements are highly reproducible.

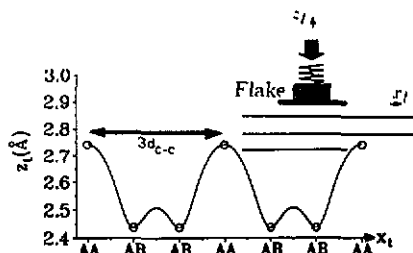


Figure 8. Vertical equilibrium position z_t of an AFM tip covered by a graphite flake, as a function of its horizontal position x_t (see inset). The flake is modelled by a monolayer of graphite. The external load (per C atom in the flake) is 10^{-9} N. The labels on the x_t axis denote the stacking between the flake and the topmost graphite layer. The solid line connecting the LDA data points is obtained from a Fourier interpolation and is explained in the text. The C–C bond length $d_{\text{C-C}}$ is 1.42 Å.

In order to determine the flake–graphite interaction, we make use of our total energy calculations for bulk graphite with AB and AA layer stacking as given in figure 1. Since the LDA calculations of $E(d)$ are performed within the LDA formalism, their validity is not limited to the elastic region of interactions. The force F between the layers is given by the derivative of the cohesive energy E with respect to interlayer spacing d , as

$$F = -\partial E(d)/\partial d. \quad (37)$$

Due to the nature of the weak interlayer coupling, we only consider pairwise interlayer interactions and use F for the flake/surface interaction. The equilibrium spacing between the layers can be obtained from $F = f_{\text{ext}}$. We find it convenient to fit the LDA data by a Morse function which converges to zero for isolated graphite

layers ($d \rightarrow \infty$). Of course, this simple description of interlayer forces breaks down at very large pressures (corresponding to $F > 10^{-8}$ N). In this force region, not discussed in this paper, the interlayer spacings become comparable to the in-layer bond length $d_{\text{C-C}} = 1.42$ Å and we expect large changes of hybridization, buckling and a transition to the diamond structure [17].

Figure 8 shows the expected corrugation for an AFM tip covered by a graphite flake and for a load (per C atom in the flake) $f_{\text{ext}} = 10^{-9}$ N. The continuous line connecting the LDA data points in figure 8 has been obtained from a Fourier expansion of the force field over the reciprocal lattice. We kept only the lowest components of this expansion and determined the expansion coefficients from the LDA results for the high-symmetry AA and AB geometries. Since the present lower limit on vertical resolution is $\Delta z_t \gtrsim 0.05$ Å, the difference $\Delta z_t \approx 0.2$ Å between the 'on-top site' (corresponding to the AA stacking) and the 'hollow site' (corresponding to the AB stacking) can easily be detected. Figure 8 suggests, however, that two adjacent AB sites can barely be distinguished at this load. In this case, the AFM would not be capable of distinguishing individual carbon atoms and the AFM image would reflect only a triangular lattice with a lattice constant of $3d_{\text{C-C}}$. Our calculated corrugations of about 0.2 Å are in very good agreement with the experimental values (0.1–0.3 Å) of Meyer *et al* [3]. At higher loads, much higher corrugations (of several angstroms) are observed. We speculate that in this load region, the tip–substrate interaction may be destructive and/or reflect the effect of atomic-scale friction between tip and substrate. It is clear that an additional orientational misalignment between the flake and the substrate would decrease this resolution. Since the rotated flake may be incommensurate with the graphite substrate, or commensurate in a very large unit cell, such orientational misalignment could also lead to superstructures in AFM images.

5. Summary and conclusions

In conclusion, we developed a first-principles theory for the atomic force microscopy (AFM) of layered elastic materials. This theory uses a new approach which combines the *ab initio* density functional formalism and continuum elasticity theory. We applied this theory to graphite with and without intercalant impurities and quantitatively determined local distortions in the vicinity of the AFM tip as a function of the applied load. Using this formalism, we investigated the effect of a finite-size tip on the substrate distortions and the resulting AFM image. In the case of an 'atomically sharp' AFM tip we concluded that AFM is capable of determining *local* changes of the surface rigidity and of measuring the healing length of graphite in the vicinity of intercalant impurities or other defects. In the case of a graphite flake attached to the tip we showed that the AFM image shows a triangular lattice with a lattice constant of $3d_{\text{C-C}}$; individual carbon atoms can be barely resolved. The graphite flake also helps to distribute the AFM load over a large surface area. In this way it is possible to observe atomic structures at AFM loads as large as 10^{-7} N without destroying the surface.

Acknowledgments

We thank Professor M F Thorpe, as well as Dr J Gales and Y Wang from Michigan State University for stimulating discussions. We also thank Dr H Heinzlmann and

Dr E Meyer from the AFM/STM group of the University of Basel for many helpful suggestions. GO acknowledges partial financial support from the Swiss National Foundation and Kommission zur Förderung der wissenschaftlichen Forschung. DT acknowledges partial financial support from the Office of Naval Research (Grant Number N00014-90-J-1396) and SDM acknowledges support from the National Science Foundation (MRG Grant Number 8514154).

References

- [1] Binnig G, Quate C F and Gerber Ch 1986 *Phys. Rev. Lett.* **56** 930
- [2] Binnig G, Gerber Ch, Stoll E, Albrecht T R and Quate C F 1987 *Europhys. Lett.* **3** 1281
- [3] Meyer E, Heinzelmann H, Grütter P, Jung Th, Weisskopf Th, Hidber H R, Lapka R, Rudin H and Güntherodt H-J 1988 *J. Microsc.* **152** 269
- [4] Albrecht T R and Quate C F 1987 *J. Appl. Phys.* **62** 2599
- [5] Rugar D and Hansma P 1990 *Phys. Today* **43** 23
- [6] Binnig G, Rohrer H, Gerber Ch and Weibel E 1982 *Phys. Rev. Lett.* **49** 57
- [7] Batra I P and Ciraci S 198 *J. Vac. Sci. Technol. A* **6** 313
- [8] Abraham F F, Batra I P and Ciraci S 1988 *Phys. Rev. Lett.* **60** 1314
- [9] Abraham F F and Batra I P 1989 *Surf. Sci.* **209** L125
- [10] Tománek D, Overney G, Miyazaki H, Mahanti S D and Güntherodt H-J 1989 *Phys. Rev. Lett.* **63** 876; 1989 *Phys. Rev. Lett.* **63** 1896 (erratum)
- [11] Lee S, Miyazaki H, Mahanti S D and Solin S A 1989 *Phys. Rev. Lett.* **62** 3066
- [12] Hohenberg P and Kohn W 1964 *Phys. Rev.* **B136** 864
- [13] Kohn W and Sham L J 1965 *Phys. Rev.* **140** A 1133
- [14] Hamann D R, Schlüter M and Chiang C 1979 *Phys. Rev. Lett.* **43** 1494
- [15] Hedin L and Lundqvist B J 1971 *J. Phys. C: Solid State Phys.* **4** 2064
- [16] Tománek D and Louie S G 1988 *Phys. Rev. B* **37** 8327
- [17] Fahy S, Louie S G and Cohen M L 1986 *Phys. Rev. B* **34** 1191
- [18] Chadi D J and Cohen M L 1973 *Phys. Rev. B* **8** 5747
- [19] Komatsu K and Nagamiya T 1951 *J. Phys. Soc. Japan* **6** 438
- [20] Gradshteyn I S and Ryzhik I M 1981 *Tables of Series, Products, and Integrals* (Thun: Verlag Harri Deutsch)
- [21] Overney G, Zhong W and Tománek D 1992 in preparation
- [22] Zabel H 1990 *Graphite Intercalation Compounds I (Springer Series in Materials Science 14)* ed H Zabel and S A Solin (New York: Springer)
- [23] Chan C T, Ho K M and Kamitakahara W A 1987 *Phys. Rev. B* **36** 3499
- [24] Chan C T, Kamitakahara W A, Ho K M and Eklund P C 1987 *Phys. Rev. Lett.* **58** 1528
- [25] Anselmetti D, Wiesendanger R and Güntherodt H-J 1989 *Phys. Rev. B* **39** 11135
- [26] Anselmetti D, Geiser V, Overney G, Wiesendanger R and Güntherodt H-J 1990 *Phys. Rev. B* **42** 1848
- [27] Meyer E private communications
- [28] Goodman F O and García N 1991 *Phys. Rev. B* **43** 4728
- [29] Anders M and Heiden C 1990 *Fifth Int. Conf. Scanning Tunneling Microscopy and NANO I (Baltimore, 1990)* poster
- [30] Zhong W, Overney G and Tománek D 1991 *Europhys. Lett.* **15** 49
- [31] Mamin H J, E Ganz, D W Abraham, R E Thomson and J Clarke 1986 *Phys. Rev. B* **34** 9015
- [32] Tománek D, Louie S G, Mamin H J, Abraham D W, Thomson R E, Ganz E and Clarke J 1987 *Phys. Rev. B* **35** 7790
- [33] Soler J M, Baro A M, García A N and Rohrer H 1986 *Phys. Rev. Lett.* **57** 444
- [34] Pethica J B 1986 *Phys. Rev. Lett.* **57** 3235
- [35] Gould S A C, Burke K and Hansma P K 1989 *Phys. Rev. B* **40** 5363